Supplementary Information for

High-Throughput Diffuse Electron Projection Lithography

Weilong Wu[1,#], Yang Li[1,#], Shuyu Mao[1], Fangyuan Zhan[1], Yuqiang Yu[1], Dan Su[2], Panqin Sun[2], Bingjie Wang[1], Taoyuan Zhu[1], Ruixue Ding[1], Ye Zhao[1], Kechang Zhang[1], Tong Zhang[2], Zhiwei Li[1,*], Qing Chen[1], Xianlong Wei[1,*]

[1]*Key Laboratory for the Physics and Chemistry of Nanodevices, School of Electronics, Peking University, Beijing 100871, China*

[2]*School of Electronic Science and Engineering, Southeast University, Nanjing 210096, China*

[#] These authors contributed equally

[*] Corresponding authors. Email: weixl@pku.edu.cn, lzw111@pku.edu.cn

Supplementary Note 1. Blocking capability of Au nanofilms for high-energy electrons

In this work, the mask of gold nanoparticles functions primarily through its robust physical blocking capabilities to effectively suppress electron penetration, thereby shielding the underlying resist from exposure. To validate its efficacy as a blocking layer, we employed Monte Carlo (MC) simulations to evaluate the penetration of energetic electron beams (2–10 keV) through Au nanofilms with uniform thicknesses (see Methods), where trajectories of 500 electrons were calculated for each nanofilm thickness. The simulation results reveal that the electron attenuation induced by the Au nanofilms exhibits two aspects. First, the transmission ratio, defined as the ratio of the number of transmitted electrons to that of total incident electrons, decreases with increasing nanofilm thickness (Fig. S1a). Strong scattering of electrons by heavy gold atoms causes large-angle trajectory deflections and backscattering. Consequently, the number of transmitted electrons decreases with increasing nanofilm thickness, at a faster rate for lower electron energies. Second, the kinetic energy of the transmitted electrons is decreased (Fig. S1b). Through inelastic scattering within the film, the kinetic energy of the transmitted electrons is substantially attenuated. Quantitatively, for a 20-nm-thick Au film exposed to a 5 keV incident beam, the transmission ratio drops to 54%, with the average kinetic energy of the transmitted electrons attenuated to 3.99 keV.

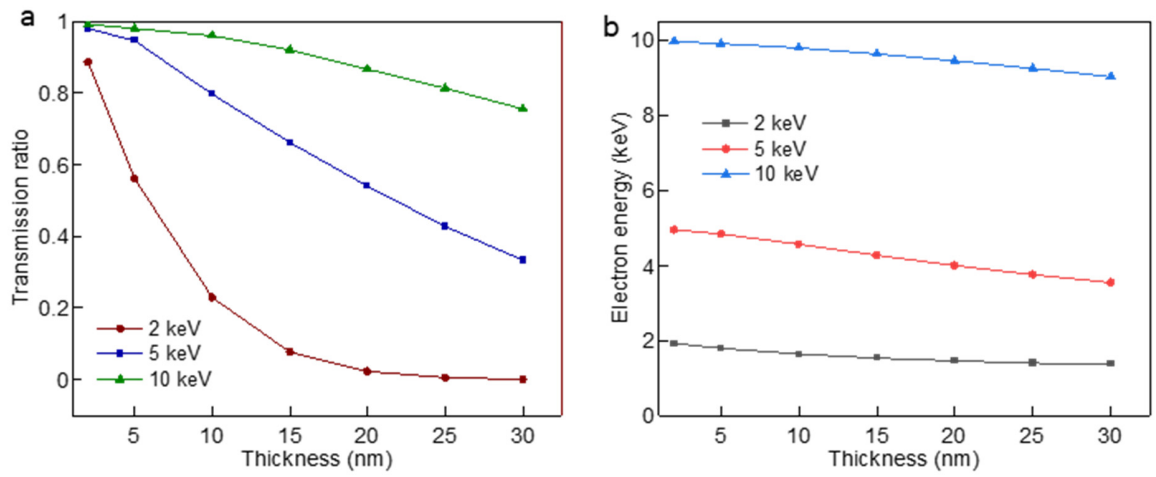

Supplementary Fig. S1 | Monte Carlo simulations of electron penetration through Au nanofilms. **a**, transmission ratio varying with nanofilm thickness. **b,** the average energy of transmitted electrons varying with nanofilm thickness. Incident beam energies of 2 keV, 5 keV and 10 keV are considered.

Supplementary Note 2. Evaluation on spatial distribution of diffuse electron sources

To quantitatively evaluate the spatial distribution of diffuse electron sources, we introduce the nearest neighbor index (NNI) to characterize the spatial distribution of diffuse electron sources. The spatial distributions of diffuse electron sources were first obtained from Monte Carlo simulations (see Methods), where trajectories of 10,000 electrons uniformly injected into air from a 2×2 array of 1-mm-wide and 1-mm-spaced membrane windows were simulated. The evolution of spatial distributions with moving distance in air was evaluated using the NNI analysis implemented in MATLAB.

The NNI is defined as the ratio between the observed mean nearest-neighbour distance $\bar{r}_{\mathrm{obs}}$ and the expected mean distance under complete spatial randomness (CSR) corresponding to a Poisson point process:

$$R = \frac{\bar{r}_{obs}}{\bar{r}_{exp}} = \frac{\frac{1}{N}\sum_{i=1}^{N} r_{\min,i}}{\frac{1}{2\sqrt{\rho}}} \tag{1}$$

, where N is the total number of simulated electrons, $r_{\min,i}$ is the distance from electron i to its nearest neighbor, and ρ is the average electron density. While $R < 1$ implies clustered distribution and $R > 1$ implies regular distribution, $R \sim 1$ implies complete spatial randomness (CSR).

To mitigate the bias introduced by long-range scattered electrons (outliers) on the spatial distribution analysis, a filtering procedure based on Mahalanobis distance (D_M) was implemented. For each simulated electron position $\mathbf{x}_i$, D_M is defined as:

$$D_M(\mathbf{x}_i) = \sqrt{(\mathbf{x}_i - \boldsymbol{\mu})^T \boldsymbol{\Sigma}^{-1} (\mathbf{x}_i - \boldsymbol{\mu})} \tag{2}$$

where $\boldsymbol{\mu}$ and $\boldsymbol{\Sigma}$ denote the mean position vector and the covariance matrix of the entire electron point cloud, respectively. $\boldsymbol{\Sigma}$ characterizes the spatial spread and orientation of the scattered electron cluster. Points lying outside the 95% confidence ellipse (determined from the chi-square distribution) were classified as outliers and excluded from the area calculation to ensure statistical robustness.

After removal of outliers via a filtering procedure based on Mahalanobis distance, the remaining core electrons with the number of N_{core} were used to construct a convex hull. The effective area A_{eff} of diffuse electron sources was defined as the area of this convex hull. The average electron density was calculated as:

$$\rho = \frac{N_{\mathrm{core}}}{A_{\mathrm{eff}}} \tag{3}$$

This procedure ensures that the estimated density reflects the intrinsic local distribution of scattered electrons, independent of the global container geometry.

The evolution of spatial distributions and NNI of diffuse electron source with moving distance in air is shown in Supplementary Fig. S2. The evolution of the NNI index directly quantifies the spatial randomization and homogenization induced by air scattering. At the initial emission plane (Z = 0 mm), the point distribution exhibits a NNI of R=0.66, indicating strong spatial clustering. As scattering in air progresses, the electron distribution becomes increasingly uniform. At Z = 5.5 mm, the NNI increases to R=0.95, which is statistically indistinguishable from unity (CSR). This demonstrates that the scattering scheme effectively suppresses structural clustering, yielding a quasi-Poisson continuous electron distribution.

The transition from R=0.66 to R=0.95 represents a fundamental increase in configurational entropy of the system. Air molecule scattering acts as an intrinsic de-clustering mechanism, driving the initially structured emission pattern toward a statistically unbiased and spatially homogeneous state.

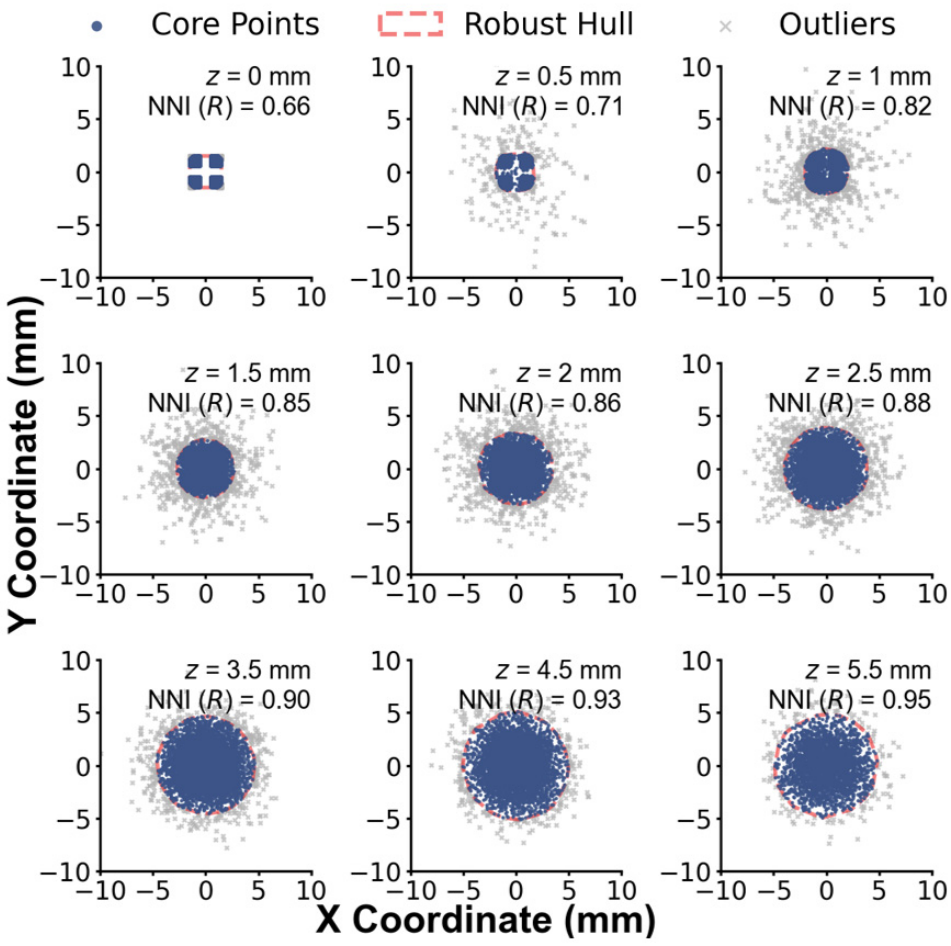

Supplementary Fig. S2 | Simulated spatial distributions of diffuse electron sources and the nearest neighbor index analysis at different distance (*Z*) in air. An initial energy of 20 keV was assumed for electron injected into air.

Supplementary Note 3. Preparation of the contact mask of Au nanoparticle monolayers

In this work, we employ a self-assembly and transfer-printing strategy to directly print Au nanoparticle monolayers onto the resist, serving as a conformal contact mask for DEPL. The preparation proceeds in three steps:

(I) Self-assembly. The critical first step is the generation of a wafer-scale, hexagonally close-packed Au nanoparticle monolayer. We utilize cetyltrimethylammonium bromide (CTAB)-capped Au nanoparticles and modify their surface with 1H,1H,2H,2H-perfluorodecanethiol (PFT) to induce a rapid assembly. Facilitated by strong Au–S covalent bonding, PFT introduces abundant superhydrophobic trifluoromethyl (-CF_3) groups, inducing a hydrophilic-to-hydrophobic transition and conferring a high contact angle of up to 132° on the nanoparticles. This surface modulation effectively eliminates the kinetic barrier to interfacial adsorption, triggering spontaneous assembly at the ethanol/n-hexane biphasic interface within 5 s (Fig. S3a). Driven by intermolecular forces, the nanoparticles organize into a dense, highly ordered monolayer superlattice, strictly precluding the formation of multilayer aggregates or loose-packing defects.

(II) Transfer. The assembled Au nanoparticle monolayer is subsequently transferred onto a patterned polydimethylsiloxane (PDMS) stamp, forming a designed pattern. The PDMS soft stamp is replicated from a reusable hard master template pre-fabricated via electron-beam or ultraviolet lithography. Supplementary Fig. S3b-c show scanning electron microscopy (SEM) image of the PDMS stamp with the patterns of periodic circles.

(III) Printing. Finally, the PDMS stamp prints the patterned Au nanoparticles onto the resist, creating a large-area, uniform mask in direct contact with the resist. By exploiting the robust interfacial adhesion between the Au nanoparticles and the resist layer, the transfer process achieves near-unity efficiency (~100%) within 1 min at 100 °C [1, 2]. In contrast to the discrete hard masks conventionally used in proximity lithography, our self-assembled masks are integrated directly onto the resist. This conformal contact fundamentally eliminates intervening air gaps, thereby effectively suppressing the resolution degradation that typically plagues proximity lithography. [3]

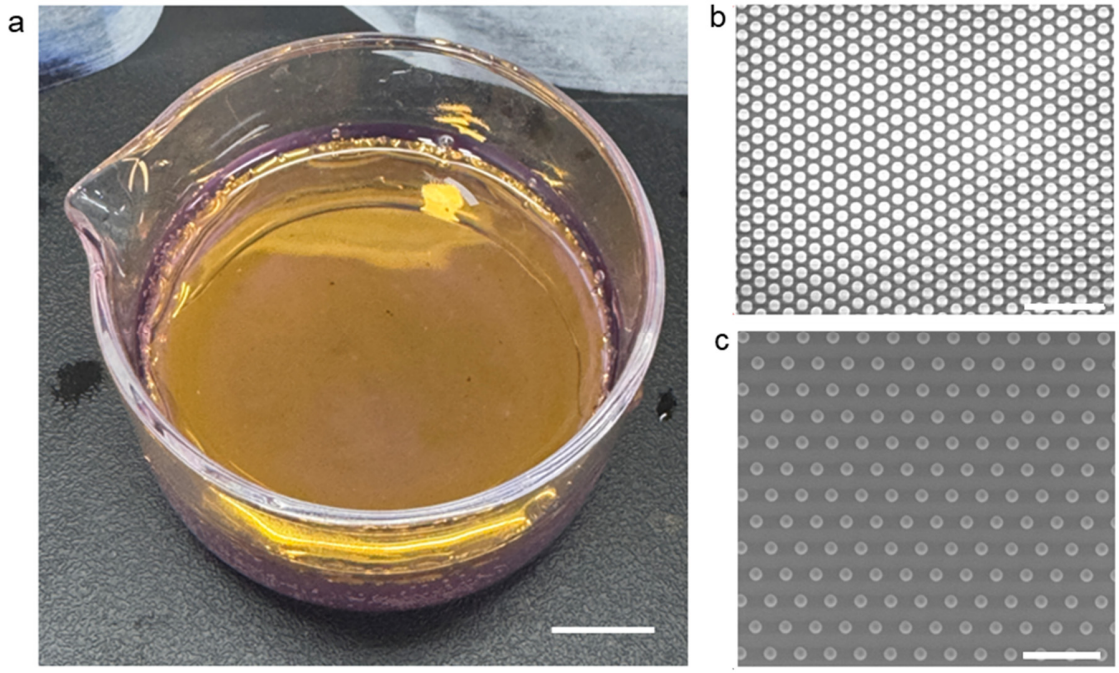

Supplementary Fig. S3 | Preparation of the contact mask of Au nanoparticle monolayers. a, Photograph of self-assembled Au nanoparticle monolayers at the ethanol/n-hexane biphasic interface. **b**, SEM image showing a PDMS stamp with patterns of periodic circles with a period of 500 nm and a diameter of 240 nm. **c**, SEM image showing a PDMS stamp with patterns of periodic circles with a period of 8 μm and a diameter of 3 μm. Scale bars, 1 cm (a), 2 μm (b), 20 μm (c).

Supplementary Note 4. Preparation of multiscale pattern masks

Multiscale patterns are characterized by hierarchical architectures with feature sizes spanning multiple orders of magnitude, effectively bridging the nanometer/micrometer to millimeter/centimeter regimes [4]. Nevertheless, the scalable fabrication of these multiscale architectures poses a formidable technical challenge, demanding exceptionally robust and large-scale manufacturing capabilities. To demonstrate our stable manufacturing capability, we fabricated a multiscale pattern mask of the Chinese characters for 'Peking University' via an intaglio-assisted transfer printing approach (Supplementary Fig. S4a). First, a rigid metal stencil (e.g., copper or stainless steel) fabricated via laser-cutting from a computer-aided design (CAD) layout (Supplementary Fig. S4b and c), served as the macroscopic template and was heated to 100 °C. An Au nanoparticle-coated PDMS stamp (prepared as described in Supplementary Note 3) was then pressed against this heated stencil under a pressure of ~ 5×10^4 N/m^2 for 10 s. Upon separation, the Au nanoparticles in direct contact with the solid regions of the stencil were adhered to the metal. Conversely, the Au nanoparticle monolayer corresponding to the hollowed-out regions remained intact on the PDMS. This subtractive process selectively removed the redundant Au nanoparticles, precisely delineating the macroscopic Chinese characters for 'Peking University' on the stamp. Finally, the patterned PDMS was pressed onto a silicon wafer (~ 1×10^4 N/m^2, 1 min) to transfer the predefined characters, yielding a hierarchical structure that exhibits well-defined features at both the macroscopic and microscopic scales (Fig. 4e).

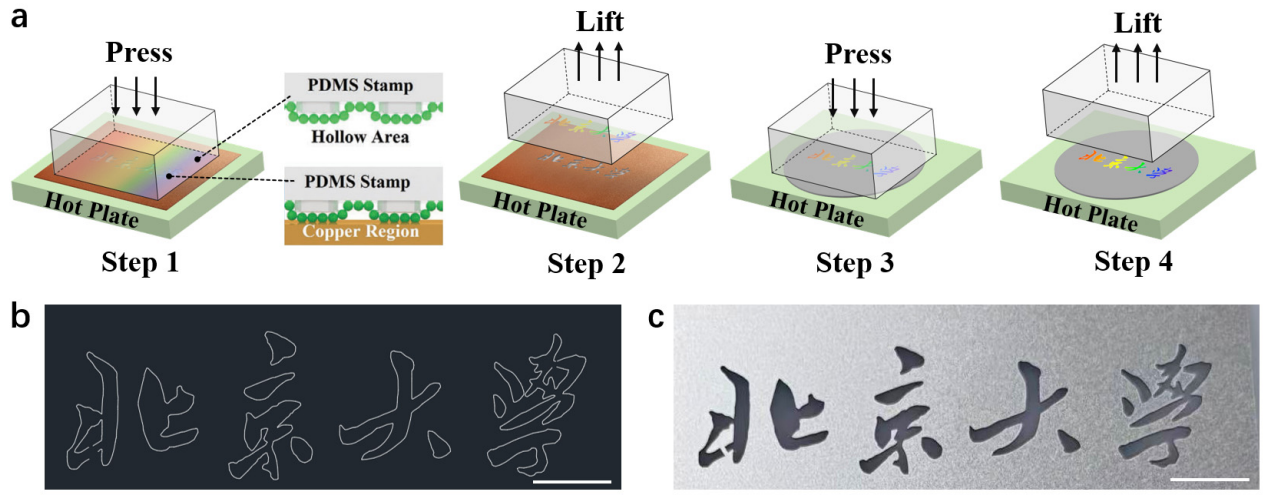

Supplementary Fig. S4 | Fabrication of multiscale pattern masks via intaglio-assisted transfer printing. a, Schematic illustration of the intaglio-assisted transfer printing process. **b,** Computer-aided design (CAD) layout of the macroscopic pattern of Chinese characters for 'Peking University'. **c,** Optical image of the laser-cut stencil template corresponding to the design in b. Scale bars: 1 cm (b, c).

Supplementary Note 5. Electron emission capability of the Ir-Y_2O_3 electron emitter

To characterize the electron emission capability of an Ir-Y_2O_3 electron emitter used in Fig. 4 (Supplementary Fig. S5a), it was placed inside a vacuum chamber and tested according to the circuit diagram shown in Supplementary Fig. S5b. A voltage (V_{emi}) was applied across the electron emitter, causing the thermionic electron emission. A metal plate with a positive voltage (V_{acc}) of 500 V was positioned 15 mm above the electron emitter to serve as a collector for the emission current (I_{emi}). The emission current measured at the collector increased rapidly with V_{emi} and exceeded 600 mA (Supplementary Fig. S5c), which is much higher than the electron current required for high throughput electron lithography.

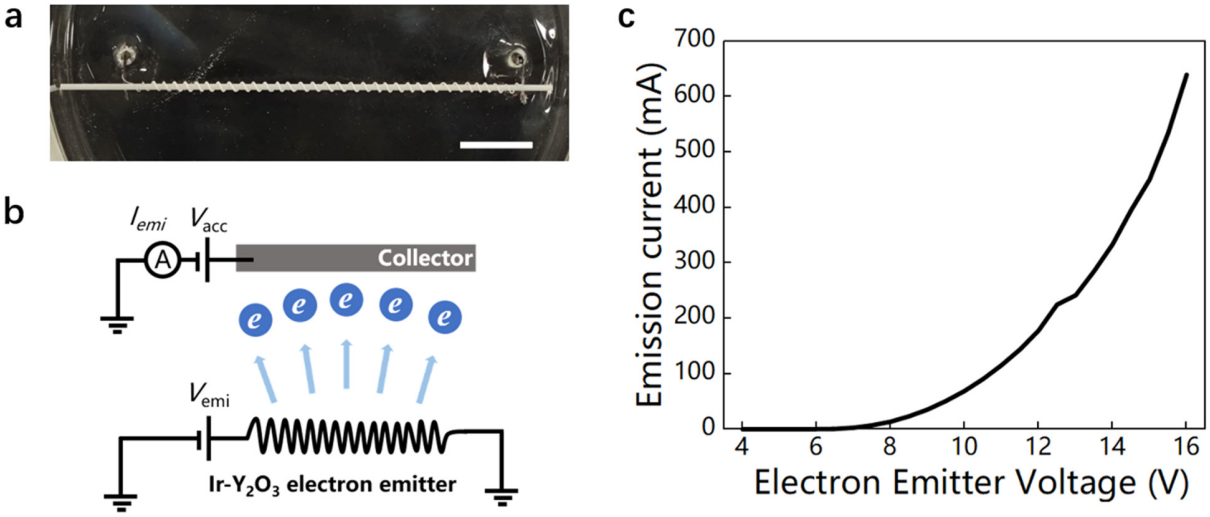

Supplementary Fig. S5 | Emission performance of the Ir-Y_2O_3 electron emitter in Fig. 4. a, Photograph of the Ir-Y_2O_3 electron emitter, which is a helical Ir filament coated with Y_2O_3 layer and entwines around a quartz rod to prevent deformation. Scale bar: 1 cm. **b,** Schematic of electron emitter performances test in a vacuum chamber. A voltage (V_{emi}) is applied to the electron emitter, causing the thermionic emission of electrons. A metal plate with a positive voltage (V_{acc}) of 500 V is positioned 15 mm above the electron emitter to serve as a collector for the emission current (I_{emi}). **c,** Plot of measured emission current versus electron emitter voltage (V_{emi}). The emission current increases rapidly with V_{emi} and can exceed 600 mA.

Supplementary Note 6. Wafer-scale fabrication of Si_3N_4 membrane window chips

The Si chips with Si_3N_4 membrane windows were fabricated from a 4-inch silicon wafer with 200 nm Si_3N_4 layers deposited on both sides. First, by photolithographic patterning and reactive ion etching (RIE), the upper Si_3N_4 layer was partially removed, exposing the underlying silicon for electrical conduction. Second, an alkaline protective coating (ProTEK® B3 Coating) was spin-coated on the upper side of the wafer to protect the top-side membrane during subsequent KOH etching. Third, by photolithographic patterning and reactive ion etching (RIE), the bottom Si_3N_4 layer was selectively etched off to expose underlying Si for KOH etching. The exposed Si regions showed the arrays of 1.5 mm-wide and 1.0 mm-spaced squares. The Si in the exposed regions was then etched off through the entire thickness in KOH solution, exposing the Si_3N_4 membrane on the upper side as membrane windows. Finally, the 4-inch wafer was laser-diced into individual chips, shown in Supplementary Fig. S6b-e, and then the B3 Coating was stripped using isopropanol and acetone to release membrane windows.

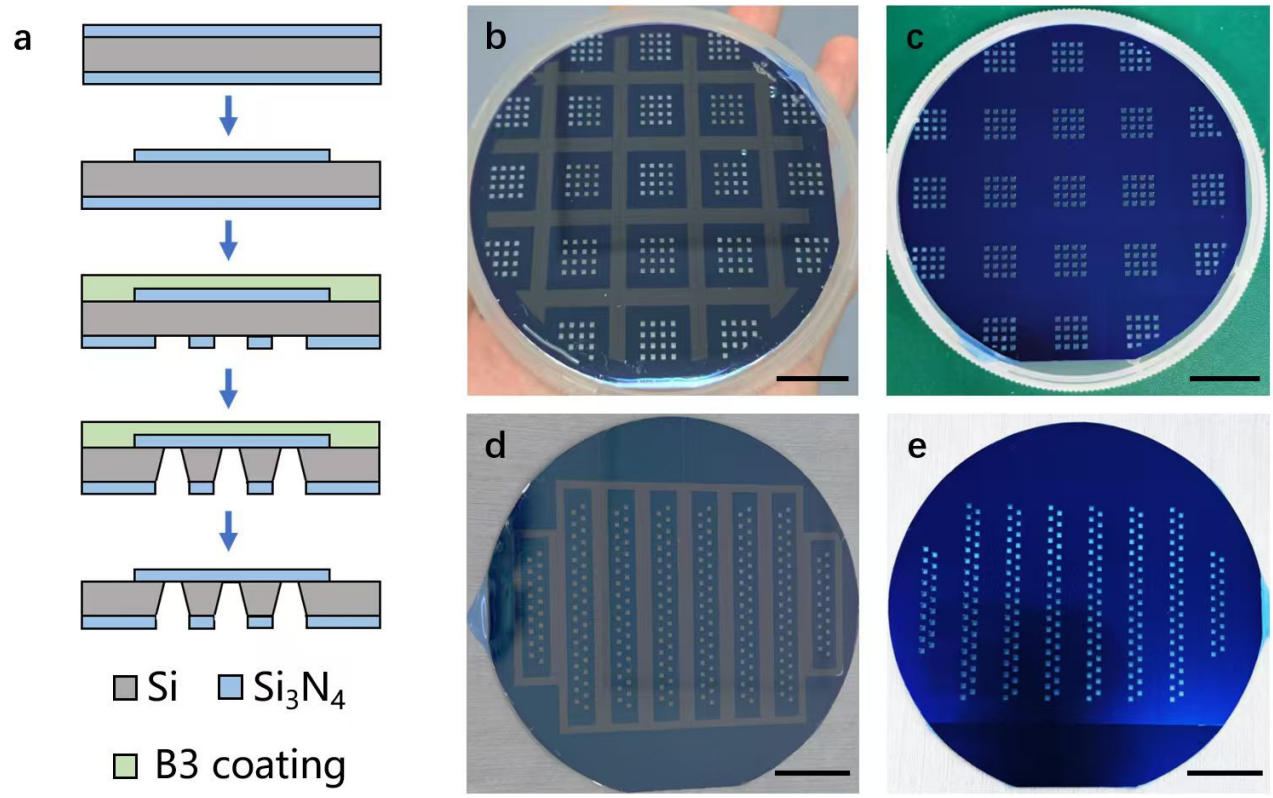

Supplementary Fig. S6 | Wafer-scale fabrication of Si chips with Si_3N_4 membrane windows. a, Schematic process flow of fabricating Si chips with Si_3N_4 membrane windows. **b, c,** Photographs of both sides of wafer-scale fabricated Si chips with an array of 4 × 4 Si_3N_4 membrane windows. **d, e,** Photographs of both sides of wafer-scale fabricated Si chips with two rows of Si_3N_4 membrane windows. Scale bars: 2 cm in b-e.

Supplementary Note 7. Home-made setup for DEPL

The setup for DEPL is a cost-effective and compact system compared with traditional electron lithography systems, as neither complex electron optics system nor ultrahigh vacuum system is required. A home-made setup for a DEPL system is shown in Supplementary Fig. S7. It mainly consists of a diffuse electron source, a vacuum system for maintaining the vacuum required by the electron emitter, a three-axis translation stage equipped with a brushless motor for fixing and scanning the wafer to be exposed, and a high voltage source for driving electron emission and accelerating electrons. The distance between the membrane windows and the wafer can be precisely adjusted by the translation stage. For wafer-scale lithography, the wafer was moved across the diffuse electron source at a constant speed driven by the translation stage.

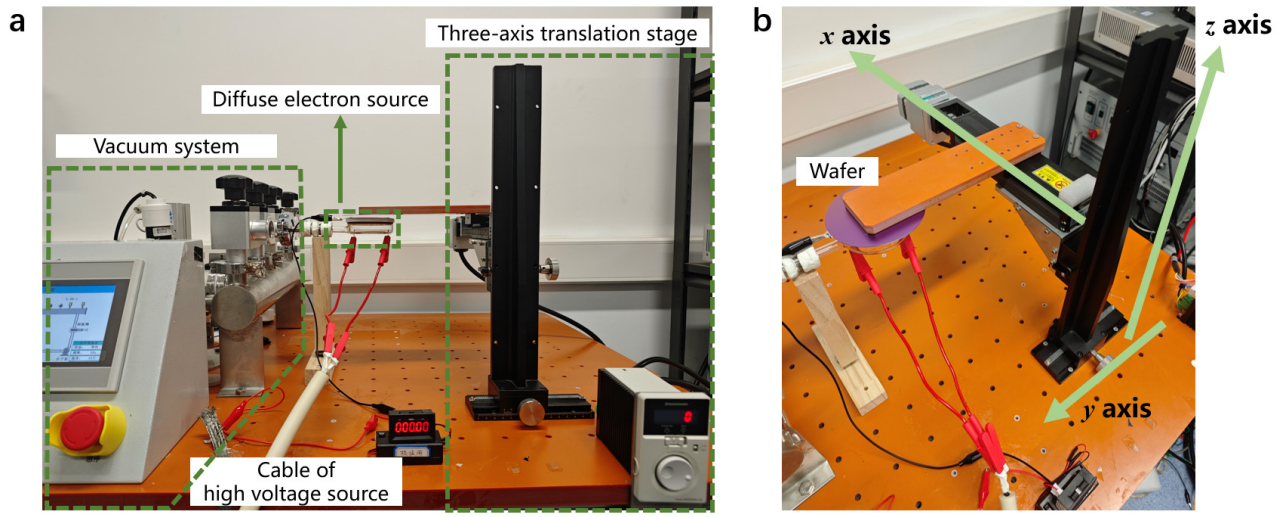

Supplementary Fig. S7 | Experimental setup of DEPL. a, Photograph of the setup. The setup mainly consists of a diffuse electron source (see details in Fig. 4b), a vacuum system for maintaining the vacuum required by the electron emitter (~10^{-3} Pa), a high voltage source for driving electron emission and accelerating electrons, and a three-axis translation stage for fixing and scanning the wafer to be exposed. **b,** Photograph of the three-axis translation stage. The three-axis translation stage consists of y- and z-axes adjusted via lead screws manually and an x-axis driven by a brushless motor. The motorized x-axis is controlled to move at a constant speed, enabling the wafer to be uniformly scanned across the diffuse electron source.

Reference

1. Feng, X. et al. Competing Fracture in Kinetically Controlled Transfer Printing. *Langmuir* **23**, 12555–12560 (2007).
2. Meitl, M. A. et al. Transfer printing by kinetic control of adhesion to an elastomeric stamp. *Nat. Mater.* **5**, 33–38 (2006).
3. Lu, Y. & Lal, A. Vacuum-Free Self-Powered Parallel Electron Lithography with Sub-35-nm Resolution. *Nano Lett.* **10**, 2197–2201 (2010).
4. Begley, M. R., Gianola, D. S. & Ray, T. R. Bridging functional nanocomposites to robust macroscale devices. *Science* **364**, eaav4299 (2019).